Acta Biomaterialia xxx (xxxx) xxx

Contents lists available at ScienceDirect

Acta Biomaterialia

journal homepage: www.elsevier.com/locate/actbio

Full length article

Balancing stability and cleavability of magnetoelectric nanovesicles for wireless and noninvasive deep brain stimulation in epilepsy therapy

Yiran Chen [a,b,1], Meng Xiao [c,d,1], Yage Sun [e], Lu Wang [d], Zhou Li [c,f,*], Fengying Dai [a,b,**]

[a] State Key Laboratory of Advanced Separation Membrane Material, National Center for International Joint Research on Separation Membranes, School of Material Science and Engineering, Tiangong University, Tianjin 300387, China
[b] Cangzhou Institute of Tiangong University, Cangzhou 061000, China
[c] Vita Tech Innovation Center, Tsinghua Changgung Hospital, School of Clinical Medicine, Tsinghua University, Beijing, 100084, China
[d] Beijing Institute of Nanoenergy and Nanosystems, Chinese Academy of Sciences, Beijing, 101400, China
[e] School of Material Science and Engineering, Tianjin Key Laboratory of Composite and Functional Materials, Tianjin University, Tianjin 300350, China
[f] School of Biomedical Engineering, Tsinghua University, Beijing 100084, China

ARTICLE INFO

Keywords:
Polymer vesicles
Magnetoelectric nanoparticles
Epilepsy
Noninvasive neuromodulation
Cleavability

ABSTRACT

Polymeric vesicles hold considerable promise as noninvasive delivery platforms for magnetoelectric nanoparticles (MENPs). This strategy enables wireless and noninvasive neural stimulation and offers effective therapeutic avenues for epilepsy, representing a translatable bench-to-bedside pathway for deep-brain magnetoelectric stimulation. However, polymer vesicles have not been widely explored for delivering MENPs in neurostimulation. A key challenge is balancing the structural stability of magnetoelectric vesicles during delivery with their rapid, on-demand cleavage at the target site, which is particularly paramount and challenging for epilepsy treatment. It is conceivable that the ROS-cleavable design could, in principle, contribute to a more localized stimulation profile and potentially help mitigate off-target effects. Following vesicle disruption, the slow release of MENPs might, under favorable conditions, result in some reduction of polymeric charge shielding, which could conceivably have a bearing on magnetoelectric stimulation performance. Amorphous bottlebrush poly(D,L-lactic acid)-dextran (PDLLA-Dextran) vesicles were developed with systemic delivery stability, and their ROS-responsive cleavage capacity may be preliminarily considered as one possible factor that could influence the spatial distribution of MENP release. Prussian blue staining confirmed their preferential accumulation in inflammatory hippocampal and cortical regions as distinct microclusters, which enhanced magnetoelectric transduction. Electroencephalography and c-Fos mapping demonstrated significant suppression of pathological network hypersynchrony in epileptic rats. These vesicles offer a versatile strategy for wireless, noninvasive neuromodulation, with significant translational potential for deep-brain stimulation therapies in epilepsy and related neurological disorders.

Statement of Significance: About one-third of focal epilepsy patients don't respond to medication, and current deep-brain stimulation implants or injections are invasive and imperfectly targeted. MENPs provide wireless electrical stimulation powered by external magnetic fields; however, their limited colloidal stability and constrained spatial control have impeded their clinical translation. We introduce amorphous bottlebrush PDLLA–dextran vesicles that stabilize MENPs during systemic delivery yet rapidly disassemble in reactive-oxygen-species (ROS)–rich epileptic microenvironments. This design addresses a critical trade-off between circulation stability and stimulus-responsive release, thereby facilitating more comprehensive MENP exposure for enhanced magnetoelectric charge generation under an external magnetic field. The platform promotes minimally invasive, targeted neuromodulation and may be broadly applicable for deep-brain disorders where local inflammation can inform on-demand activation.

* Corresponding author at: Vita Tech Innovation Center, Tsinghua Changgung Hospital, School of Clinical Medicine, Tsinghua University, Beijing, 100084, China.
** Corresponding author at: State Key Laboratory of Advanced Separation Membrane Material, National Center for International Joint Research on Separation Membranes, School of Material Science and Engineering, Tiangong University, Tianjin 300387, China.
E-mail addresses: li_zhou@tsinghua.edu.cn (Z. Li), daifengying@tiangong.edu.cn (F. Dai).
[1] Yiran Chen and Meng Xiao contributed equally to this work and should be regarded as co-first authors

https://doi.org/10.1016/j.actbio.2026.06.048
Received 14 February 2026; Accepted 23 June 2026
Available online 24 June 2026

1. Introduction

Epilepsy is a severe neurological disorder characterized by spontaneous and recurrent seizures resulting from abnormal neuronal hyperexcitation, which carries a significant risk of sudden unexpected death and imposes substantial socioeconomic burdens. Approximately one-third of patients with focal epilepsy develop medically refractory epilepsy, making them potential candidates for surgical intervention. The standard procedure involves tunneling a lead wire subcutaneously to the carotid sheath, where platinum electrodes are then implanted around the vagus nerve. However, this therapeutic approach achieves favorable long-term efficacy in only about two-thirds of treated patients, leaving a significant proportion with inadequate seizure control [1].

The development of minimally invasive, more efficacious, and safer deep-brain stimulation (DBS) technologies represents a critical frontier in the treatment of brain disorders. While both optical and ultrasonic neuromodulation modalities face fundamental limitations in brain penetration depth, magnetically responsive micro/nano-scale neural interfaces have emerged as particularly promising for wireless neuromodulation due to their superior penetration capability [2,3]. Magnetoelectric nanoparticles (MENPs) operate through strain transfer from their magnetostrictive component to the piezoelectric phase. This process generates a localized electric field via charge separation, thereby enabling the development of non-invasive, miniaturized neural stimulators powered by external magnetic fields. Such systems hold considerable promise for targeted deep-brain stimulation in the treatment of neurological disorders [4]. Yue et al. first reported the use of MENPs to modulate brain activity in a patient with Parkinson's disease, raising the pulsed electric field sequences to levels comparable to those observed in healthy individuals [5]. However, the study did not include replicates or statistical analyses to confirm the clinical efficacy. In another study, micron-scale aggregates of MENPs were stereotactically infused into the subthalamic area of mice. These aggregates were wirelessly activated by an external magnetic field, enabling neuronal modulation both in vitro and at deep brain targets in vivo [6]. Meanwhile, Fe_3O_4@$BaTiO_3$ magnetoelectric nanochains with diameters of 300 nm and lengths on the micron-scale have been stereotactically injected into the anterior thalamic nucleus of rats [7]. These MENPs show promising potential for wireless electrical modulation in vivo. However, the advancement of these MENPs is constrained by the limited spatial reach of the stimulation, as the precision of current stereotactic methods remains insufficient for accurately targeting foci [8].

The development of MENPs is significantly impeded by their inadequate colloidal stability. This instability is evidenced by the rapid formation of micron-scale aggregates in aqueous media, which severely limits their potential for systemic delivery [9,10]. The presence of hydrophilic groups on the surface of $CoFe_2O_4$-$BaTiO_3$ (CFO-BTO) MENPs further supports the feasibility of their encapsulation and transport via polymer vesicles [11]. However, magnetoelectric vesicles capable of deep-brain stimulation therapy remain underdeveloped to date. The core scientific challenge resides in the fundamental structural design paradox of vesicles engineered for MENPs delivery. The optimal vesicles must achieve a critical balance between delivery stability and stimulus-responsive cleavability: maintaining sufficient stability to endure systemic delivery stresses (including hemodynamic shear forces, physiological dilution effects, ionic interference, and protein corona formation) [12–17], while retaining the capacity for rapid, on-demand cleavability and precise MENPs release at epileptogenic foci [18–21]. While maintaining the structural stability of magnetoelectric vesicles during delivery is crucial, the ability to achieve microenvironment-specific cleavage after brain entry is more paramount and challenging for epilepsy treatment. A rapid, Reactive Oxygen Species(ROS) cleavable mechanism is essential for enabling precise stimulation, thereby minimizing off-target toxicity to healthy neurons. Moreover, the subsequent cleavage of the vesicles ensures the complete release of MENPs, which reduces the shielding effect of the polymeric vehicle on the magnetoelectric charges and ultimately enhances magnetoelectric stimulation efficacy. Although conventional vesicles made from polymers such as poly(L-lactic acid) (PLLA) and poly (ε-caprolactone) (PCL) demonstrate high shell stability owing to their well-ordered lamellar structures, their densely crystalline domains significantly retard the kinetics of ROS-mediated cleavage. This limitation consequently diminishes their value for targeted magnetoelectric stimulation in epilepsy treatment.

Our recent investigations into amorphous bottlebrush block copolymers vesicles, specifically those based on poly(D,L-lactide) (PDLLA)-Dextran vesicles, have revealed a promising avenue for resolving this dilemma [22–27]. Herein, we explore a synthetic strategy for fabricating PDLLA-Dextran-based bottlebrush block copolymer vesicles, which is proposed to be optimized for systemic delivery of MENPs. Based on the proposed design, it is conceivable that a balance between vesicle stability and ROS-responsive cleavability might potentially be achieved. Such a balance could, in principle, offer a possible means of facilitating MENP release preferentially within epileptic inflammatory regions, although this would likely be contingent upon local microenvironmental conditions. If so, it is conceivable that this property could have a bearing on the modulation of certain neuronal ion channels, synaptic transmission, or network rhythms, though the nature and extent of such influences remain to be determined. It is hypothesized that this activity may suppress synchronized neural discharges within the epileptogenic zone, thereby offering a possible approach for non-invasive deep-brain magnetoelectric stimulation in the treatment of epilepsy (Scheme 1).

2. Materials and methods

2.1. Materials

D,L-lactide (DLLA), L-lactide (LLA), Sn-ethylhexanoate ($Sn(oct)_2$), Dextran (Dex) (M_n=2000), hydrogen peroxide (H_2O_2), dimethyl sulfoxide (DMSO), N,N-dimethylformamide (DMF), chloroform ($CHCl_3$), ethyl alcohol, oleic acid, n-hexane, lithium chloride, coumarin 6, and triethylamine (Et_3N) were purchased from Macklin Biochemical Co., Ltd. (Shanghai, China). 2-hydroxyethyl methacrylate (HEMA), pyrene, acryloyl chloride, 2-mercaptoethanol, benzyl bromide (99%), 2-mercaptoethanol, potassium hydroxide (KOH), dichloromethane (CH_2Cl_2), carbon disulffde (CS_2), 2,2′-azobis (2-methylpropionitrile) (AIBN), methanol, toluene, dodecyl dimethyl benzyl ammonium chloride (DDBAC), sodium dodecyl sulfate (SDS), sodium chloride (NaCl), sodium hydroxide (NaOH), iron(III) chloride hexahydrate, lactic acid, and citric acid (CA) were bought from HEOWNS (Tianjin, China). Barium carbonate, titanium isopropoxide, Cobalt(II) nitrate hexahydrate, and Iron(III) nitrate nonahydrate were purchased from Aladdin Biochemical Technology Co., Ltd. (Shanghai, China). Cell Counting Kit-8 (CCK8), phosphate-buffered saline, fetal bovine serum (FBS), and Fluo-4 AM were offered from Beyotime Biotechnology (Shanghai, China). Pilocarpine Hydrochloride was purchased from Yuanye Bio-Technology Co., Ltd. (Shanghai, China). DMEM, Trypsin-EDTA were purchased from Biosharp Life Sciences (Hefei, China), c-Fos protein, prussian blue staining kit, and hematoxylin-eosin (H&E) constant dye kit were purchased from Servicebio (Wuhan, China)

2.2. Characterization

The chemical structure of the polymer was characterized by ^{1}H—NMR spectroscopy (400 MHz, Bruker, Germany). The hydrodynamic diameter (D_h) and zeta potential were measured using a laser particle size analyzer (Zetasizer Nano ZS, Malvern, USA). The morphologies of the polymer nanoparticles and CFO-BTO MENPs were examined by transmission electron microscopy (TEM, G2 F20, Hitachi, Japan) operated at 200 kV, coupled with energy-dispersive X-ray spectroscopy (EDS) for elemental analysis. The crystal structures of CFO,

BTO, and CFO-BTO were analyzed by X-ray diffraction (XRD) and X-ray photoelectron spectroscopy (XPS). Magnetic hysteresis loops were measured using a vibrating sample magnetometer (VSM) and a physical property measurement system (PPMS). Ferroelectric hysteresis loops were obtained with a ferroelectric analyzer. The piezoelectric coefficient (d33) was measured using a dedicated d_{33} meter. The magnetoelectric coupling coefficient (α) was determined with a BKT-6500 magneto-electric measurement system (Beijing Xinke High-Tech Testing Co., Ltd.). Surface wettability of CFO-BTO was evaluated via contact angle measurements performed on a DSA100 instrument at room temperature.

2.3. Synthesis of acryloyl chloride-Dextran (AC-Dex2K)

AC-Dex2K was synthesized by reacting Dextran (Mn = 2000) with acryloyl chloride in the presence of triethylamine within a DMSO/DMF mixed solvent. The Dextran used had an Mn of 2000 and is therefore denoted as Dex2K. The product obtained from its reaction with acryloyl chloride is named AC-Dex2K. A solution of Dextran (3.0 g, M_n = 2000) in

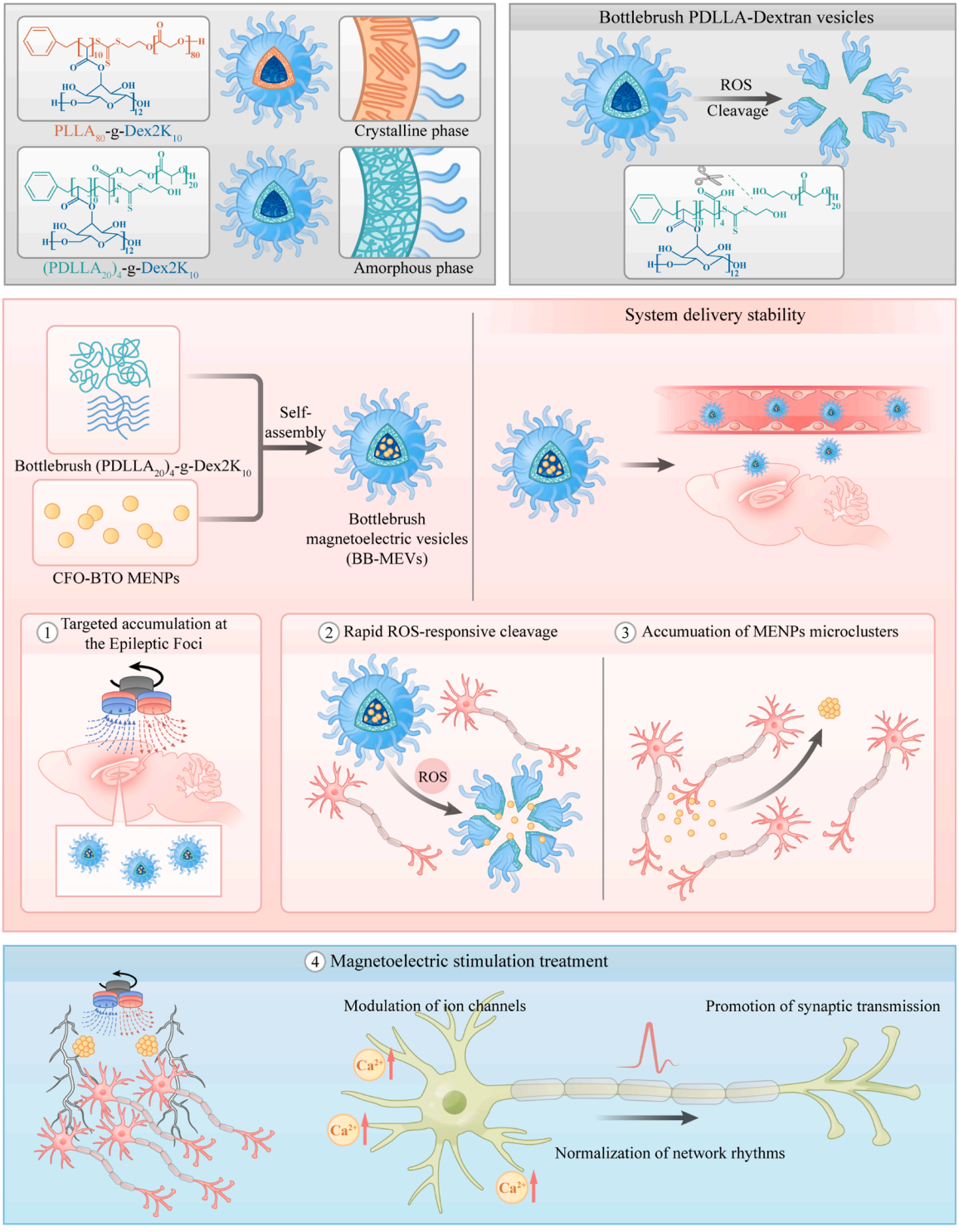

Scheme 1. Schematic illustration of amorphous bottlebrush PDLLA–Dextran vesicles serving as delivery platforms for magnetoelectric nanoparticles (MENPs) in non-invasive neuromodulation of epileptic rats.

a blended solvent of DMSO and DMF (10.0 mL, 3:1, v/v) was introduced into a 250 mL round-bottom flask. Following the complete dissolution of the Dextran, 600 μL of triethylamine was introduced. This was followed by the slow, dropwise addition of 5 mL of a DMSO solution containing acryloyl chloride (300.0 μL, 3.0 mmol) through a constant-pressure funnel while the reaction flask was maintained in an ice-water bath. The reaction was then allowed to proceed at 25 °C for 12 h. After dialyzing with a dialysis bag (MWCO = 3500 Da) for 72 h and freeze-drying, the product was obtained and named AC-Dex2K.

2.4. Synthesis of $(PDLLA_{20})_{4\ g}$-$Dex2K_{10}$

$(PDLLA_{20})_{4\ g}$-$Dex2K_{10}$ was synthesized via a two-step process involving ring-opening polymerization and RAFT-based graft-from polymerization. The degree of polymerization (DP) of the polymers and the grafting number were assessed by the characteristic peaks in their ^{1}H NMR spectra. In the nomenclature $(PDLLA_{20})_{4\ g}$-$Dex2K_{10}$, the subscripts denote the DP and the number of grafted chains, respectively, which form the basis for the polymer's name. $PDLLA_{20}$—HEMA was synthesized via ring-opening polymerization (ROP). Specifically, DLLA (2.0 g, 13.9 mmol), HEMA (156.2 mg, 1.2 mmol), and stannous octoate (400.0 μL, 1.2 mmol) were dissolved in toluene and added to a 50 mL Schlenk tube. The mixture underwent three freeze–thaw cycles and was subsequently placed under a nitrogen atmosphere. The reaction was carried out in an oil bath at 110 °C for 12 h. After polymerization, the product was dialyzed against cold methanol for 72 h, followed by dialysis in deionized water for another 72 hours to ensure complete removal of solvents. The final product $PDLLA_{20}$—HEMA was obtained as a white powder after freeze-drying, with a yield of approximately 75%.

(Benzylsulfanylthio carbonylsulfanyl) ethanol (BSTSE) was synthesized following a procedure adapted from the work of Hales [28]. Macromolecular RAFT Chain Transfer Agent $(PDLLA_{20})_4$—CTA was synthesized via the following procedure. $PDLLA_{20}$—HEMA (2.2 g, 1.3 mmol), AIBN (32.8 mg, 0.2 mmol), and BSTSE (75.0 mg, 0.3 mmol) were dissolved in 10 mL of DMSO in a 50 mL Schlenk tube. The mixture underwent three freeze–thaw cycles and was then placed under a nitrogen atmosphere. The reaction was conducted in an oil bath at 70 °C for 12 h. Upon completion, the product $(PDLLA_{20})_4$—CTA was dialyzed against deionized water for 72 h and finally freeze-dried with a yield of about 75%.

$(PDLLA_{20})_{4\ g}$-$Dex2K_{10}$ was synthesized according to the following procedure. $(PDLLA_{20})_4$—CTA (100.0 mg, 16.6μmol), AC-Dex2K (400.0 mg, 200.0 μmol), and AIBN (3.0 mg, 18.3 μmol) were dissolved in 10 mL of DMSO in a 50 mL Schlenk tube. The solution underwent three freeze–thaw cycles and was then reacted at 70 °C for 12 hours under a nitrogen atmosphere. After completion, the product was dialyzed against deionized water for 72 hours and freeze-dried, yielding approximately 80% of the final polymer. The chemical composition of the copolymer was determined based on the integrated area of the characteristic peaks in the ^{1}H NMR spectrum (Figure S1).

2.5. Synthesis of $PLLA_{80}$- g-$Dex2K_{10}$

$PLLA_{80}$-g-$Dex2K_{10}$ was synthesized via ring-opening polymerization of L-lactide using BSTSE as a chain transfer agent. The degree of polymerization (DP) of the polymers and the grafting number were assessed by the characteristic peaks in their ^{1}H—NMR spectra. In the nomenclature $PLLA_{80}$-g-$Dex2K_{10}$, the subscripts denote the DP and the number of grafted chains, respectively, which form the basis for the polymer's name. $PLLA_{80}$-g-$Dex2K_{10}$ was synthesized as previously reported [18]. L-lactide (LLA, 4.0 g, 27.8 mmol), stannous octoate (200 μL, 0.6 mmol), and BSTSE (150.0 mg, 0.6 mmol) were dissolved in 15 mL of toluene. The mixture underwent three freeze–thaw cycles and was then reacted at 110 °C for 12 hours under a nitrogen atmosphere. After reaction, the product was purified by dialysis against cold methanol followed by deionized water. The final product $PLLA_{80}$-g-$Dex2K_{10}$ was obtained as a white solid after freeze-drying, with a yield of approximately 75%. The chemical composition of the copolymer was confirmed by ^{1}H NMR spectroscopy (Figure S1).

2.6. Synthesis of CFO-BTO

CFO-BTO MENPs were synthesized via a two-step process involving hydrothermal synthesis of CFO nanoparticles followed by sol-gel coating with BTO to form a core–shell composite. Cobalt ferrite (CFO) nanoparticles were synthesized via a hydrothermal method [29]. Initially, an aqueous solution was prepared by dissolving 2 mmol of $Co(NO_3)_2{\cdot}6H_2O$ and 4 mmol of $Fe(NO_3)_3{\cdot}9H_2O$ in 40 mL of deionized water, followed by the addition of 24 mL of oleic acid. An ethanol solution of NaOH was then slowly introduced into the precursor solution under stirring. After thorough mixing, the solution was transferred into a 100 mL Teflon-lined stainless steel autoclave. The reaction was conducted in an oven at 200 °C for 12 hours. After cooling to room temperature, the resulting particles were washed repeatedly with n-hexane and ethanol to remove impurities and unreacted residues. Finally, the purified cobalt ferrite particles were obtained after drying.

CFO-BTO was synthesized via a sol–gel method [30]. The barium titanate precursor solution was first prepared by combining 30 mL of an aqueous solution containing barium carbonate (0.58 mmol) and citric acid (2.08 mmol) with 30 mL of an ethanol solution containing citric acid (20.8 mmol) and titanium isopropoxide (0.75 mmol). The mixture was subjected to sonication until a homogeneous solution was obtained. Subsequently, 0.1 g of pre-synthesized CFO nanoparticles was incorporated into the sol, and ultrasonic treatment was continued for an additional 2 hours to ensure uniform dispersion. The mixture was then stirred continuously at 60 °C until gelation occurred. Finally, the resulting gel was sintered at 700 °C in a muffle furnace to yield the CFO-BTO core-shell composite.

2.7. Preparation and stability of vesicles

Vesicles were prepared from the synthesized graft copolymers, and their stability under various conditions was evaluated. In brief, 20.0 mg of $(PDLLA_{20})_{4\ g}$-$Dex2K_{10}$ or $PLLA_{80}$-g-$Dex2K_{10}$ was fully dissolved in 2 mL of DMSO. The resulting organic solution was added dropwise into 5 mL of vigorously stirred ultrapure water to facilitate nanoparticle formation via self-assembly. Finally, the dispersion was dialyzed against ultrapure water using a dialysis membrane (MWCO 3500 Da) to remove the organic solvent.

The vesicles were evaluated for stability and ROS-responsive cleavability at a mass concentration of 2 mg/mL. The stability of vesicles was evaluated using the following procedures. The critical vesicle concentration (CVC) was determined using an F-4700 fluorescence spectrometer (Hitachi, Japan). The pyrene emission spectra were recorded from 100 to 800 nm with an excitation wavelength of 334 nm. The intensity ratio of the third (384 nm) to the first (372 nm) vibrational peaks (I_3/I_1) was plotted to determine the CVC. The structural stability of vesicles can be compromised by shear forces through both direct mechanical disruption and indirect induction of disassembly. To investigate this effect, 10 mL coumarin-loaded vesicles were circulated in a simulated vascular flow system (10 mL PBS buffer, pH=7.4) by means of a peristaltic pump. During the flow cycles, 3 mL of dialysate of the circulating fluid was extracted and analyzed using ultraviolet-visible spectrophotometry at a wavelength of 442 nm for the quantification of coumarin leakage. Surfactants and electrolytes can disrupt vesicles via competitive displacement and charge shielding. To investigate the structural stability, the vesicles were treated with sodium chloride (NaCl), the anionic surfactant sodium dodecyl sulfate (SDS), and the cationic surfactant dodecyl dimethyl benzyl ammonium chloride (DDBAC), respectively [15–17].

2.8. ROS cleavability of vesicles

The ROS-responsive cleavability of the vesicles was characterized in hydrogen peroxide solutions. Vesicles were treated with 0.5–5 mM H_2O_2, a concentration range that has been substantiated by multiple studies investigating inflammation, oxidative stress, and in vivo ROS levels in both human epilepsy and rat epilepsy models. (Supporting information 2.3)

Initially, 3 mL of $(PDLLA_{20})_4$ $_g$-$Dex2K_{10}$ vesicles dispersion were placed in 97 mL of phosphate buffer solution at 0.5 mM,1.0 mM and 5.0 mM of H_2O_2 (pH 7.4). After 72 hours, the supernatant was collected, and its transmittance was measured using an ultraviolet-visible spectrophotometer. More specifically, $(PDLLA_{20})_4$ $_g$-$Dex2K_{10}$ vesicle dispersions were placed in vials, photographed before and after the addition of H_2O_2, and subjected to dynamic light scattering analysis to confirm their ROS-responsive disintegration behavior. Finally, the particle size changes were monitored by DLS and documented photographically to illustrate the vesicle disintegration process. Furthermore, a PBS solution (pH 7.4) of the polymer at a concentration of 20 mg/mL containing 5.0 mM H_2O_2 was prepared. Aliquots were collected after 4, 8, 12, 24, 48, 72, and 96 hours of incubation. Following sedimentation, 1.0 mL of the supernatant was mixed with 2.0 mL of $FeCl_3$ solution (0.2%w/v). The ultraviolet absorption intensity of the resulting mixture was measured using a UV spectrophotometer, and the lactic acid concentration was determined via a standard calibration curve.

2.9. Preparation of MENPs-loaded pdlla bottlebrush-based vesicles (BB-MEVs)

MENPs-loaded PDLLA bottlebrush-based vesicles (BB-MEVs) were prepared by co-assembly of $(PDLLA_{20})_4$ $_g$-$Dex2K_{10}$ and CFO-BTO nanoparticles via dialysis. 20.0 mg of $(PDLLA_{20})_4$ $_g$-$Dex2K_{10}$ and 5.0 mg of CFO-BTO were dispersed in 2 mL of DMSO. 5 mL of deionized water was dropped into the copolymer solution by syringe. The solution was placed in a deionized water dialysis bag (MWCO = 3500 Da) for 72 h to obtain BB-MEVs. The freeze-dried product of the BB-MEVs dispersion was used for qualitative analysis to characterize the loading capacity. The powder was subjected to thermogravimetric testing in an air atmosphere at a temperature rise rate of 10 °C/min to a final temperature of 800 °C. The loading capacity of BB-MEVs was characterized by inductively coupled plasma spectroscopy (ICP-OES). After diluting the dispersion, microwave digestion was carried out to determine the content of Fe and Ti, and then the content was calculated by the standard curve. The loading efficiency reflects the weight proportion of MENPs in the final MENPs-loaded nanovesicle. It is calculated based on ICP-MS data as the weight ratio of MENPs to the total weight of the magnetoelectric vesicles.

2.10. In vitro assessment of neurostimulation

The neurostimulatory potential of BB-MEVs was evaluated in vitro through cell viability assays and calcium flux measurements under magnetoelectric stimulation. Previous neural stimulation research has relied on micrometer-level or millimeter-scale magnetoelectric devices. These devices can achieve resonant coupling at clinically relevant stimulation frequencies, typically between 130 and 190 Hz, for remote power delivery [3,6,8]. However, this approach inherently creates an inverse correlation between device size and achievable tissue penetration depth. Consequently, such devices require surgical implantation into brain tissue and have been unable to effectively modulate neurons within deep brain structures. However, the mechanical resonance frequency of MENPs falls within the gigahertz range, which lies far outside the clinically useful operational window. At the typical clinical stimulation frequency, MENPs operate in a non-resonant state. Although they exhibit a lower magnetoelectric response under this condition, the resulting electrical signals have been demonstrated to generate sufficient output to exceed the threshold required for effective neuromodulation [6]. Therefore, leveraging established parameters from the literature, the magnetoelectric platform described here utilizes a 220 mT DC field generated by permanent magnets, combined with a smaller 6 mT AC field oscillating at 140 Hz(Supporting Information 2.5).

The human neuroblastoma cell line, referred to as SH-SY5Y, was maintained in DMEM/F12 medium containing 10% fetal bovine serum and 1% penicillin-streptomycin at 37 °C in a humidified 5% CO_2 environment. For viability testing, cells were plated in 96-well plates at 1×10^5 cells per well and treated with BB-MEVs for 24 hours. Viability was measured using the CCK-8 kit following the manufacturer's protocol, and absorbance readings at 450 nm were taken with a Varioskan Lux microplate reader (Thermo Scientific, USA).

For magnetoelectric stimulation studies, SH-SY5Y cells were seeded in 24-well cell culture plates at a density of approximately 5×10^5 cells per well with 1 mL of culture medium. After 12 hours, the cells were digested with trypsin, centrifuged at 1000 r/min for 5 min, and subsequently resuspended in PBS. To ensure comparability across samples, the cell concentration of all samples was precisely adjusted to a uniform density of 1×10^6 cells/mL using a cell counter prior to staining. The cell suspension was loaded with 1 μM Fluo-4 AM dye and gently mixed by pipetting. The suspension was then incubated in a 37 °C incubator for 30 min in the dark, with gentle shaking performed once during incubation to ensure uniform dye loading. This step allows Fluo-4 AM to cross the cell membrane and be hydrolyzed by intracellular esterases into the negatively charged, membrane-impermeant fluorescent form Fluo-4. Following incubation, the cells were washed twice with pre-warmed assay buffer to thoroughly remove any residual extracellular dye. After centrifugation, the stained cell suspension was resuspended in 800 μL of PBS, and 50 μL of BB-MEV at a concentration of 1 mg/mL was added for magnetoelectric stimulation (AC 6 mT, 220 Hz, stimulation duration 3 min). Fluorescence signal detection was performed immediately after stimulation using 488 nm laser excitation and detection in the FL1 (530/30 nm) channel. To ensure sample comparability, a fixed number of 10^4 cells was acquired for each sample. The signals from unstained cell samples were used as the background mean fluorescence intensity for calculating the number of positive cells.

2.11. In vivo assessment of neurostimulation in a rat model of epilepsy

The neurostimulatory efficacy of BB-MEVs was evaluated in vivo using a lithium-pilocarpine-induced rat epilepsy model. BB-MEVs were administered to rats via intranasal instillation once daily at a dose of 0.48 mg vesicles/kg body weight for two consecutive days. The selection of a 120-minute magnetoelectric treatment window is based on the characteristics of the acute seizure phase in this model. This setting refers to previous literature reports on pilocarpine-induced epileptic rat models. Kevin D. et al. systematically investigated the progression of acute seizures following pilocarpine modeling. Data from Racine scale scoring and electroencephalogram root mean square analysis showed that after pilocarpine injection, animals first entered a seizure latent period of 60 min, followed by the epileptic seizure phase [31]. Our experimental observations further revealed that beyond 150 min after pilocarpine injection, the intensity of seizures in rats gradually diminished. Therefore, in this study, magnetoelectric therapy was strictly confined to within 120 min post-pilocarpin injection, during which the rats were grouped and received multiple stimulations. To ensure consistency in experimental conditions across groups, a total of 7 animals per group were ultimately selected for the experiment. Based on this inter-group comparative design, ANOVA was selected for statistical analysis. Furthermore, Tukey's post hoc test was employed to conduct pairwise comparisons between specific groups.

Thirty-five male Sprague-Dawley (SD) rats were randomly assigned to five experimental groups (n = 7 per group): the normal group, the epilepsy group, the AC field group, the BB-MEVs/2AC group, and the BB-MEVs/4AC group. In this study, five groups, including treatment and

control groups, were established with seven animals per group. Although this sample size is at the lower statistical threshold, it was carefully selected to complete all stimulations within the optimal therapeutic window. All animal experiments used the same magnetoelectric stimulation device, and treatments were completed within 120 min post-modeling. The BB-MEVs/2AC group received two stimulations, while the BB-MEVs/4AC group received four. This design took into account the possibility that two stimulations alone might be insufficient to suppress seizure activity.

To restrict the magnetic exposure to the body region, magnetic shielding was implemented using iron foil wraps, as demonstrated in Fig. 5b and Figure S10. The magnetoelectric stimulation groups were exposed to a 3-minute Alternating Current (AC) magnetic field stimulation at 6 mT and 140 Hz, delivered at 30-minute intervals. During the stimulation experiment, the behavior of the rats was observed and recorded, and seizure scores were assessed according to the Racine scale. Healthy rats were also recorded simultaneously as a reference. The number of seizures and duration time were recorded for analysis. Following completion of magnetoelectric stimulation (approximately 120 min after pilocarpine injection), one animal from each group was sacrificed for brain tissue collection and c-Fos protein staining. The remaining six animals in each group continued to be housed and subsequently underwent the open-field test and body weight monitoring. Rats were subjected to a 10-minute open-field experiment on a camera controlled by Mouse Track Application (version 1.0, Stoelting, Wooddale, Illinois, USA), and their behavior in the open field was recorded and analyzed. Electroencephalogram (EEG) recordings were performed using a multichannel in vivo recording system (Cereplex Direct, Blackrock Microsystems) with electrodes implanted in the rat brain.

Brains were harvested and fixed overnight in 4% paraformaldehyde at 4 °C, followed by paraffin embedding and sectioning at 4 μm for subsequent Nissl and Prussian blue staining. For c-Fos immunofluorescence, paraffin-embedded sections were incubated overnight at 4 °C with a primary anti-c-Fos antibody. After washing with PBS, the sections were incubated with a CY3-conjugated goat anti-mouse IgG secondary antibody under light-protected conditions. Nuclei were counterstained with DAPI. Finally, sections were mounted and imaged using fluorescence filters specific to the DAPI and CY3 channels. Hematoxylin and eosin (H&E) staining was carried out on tissue sections obtained from major organs. After paraffin embedding and sectioning, the samples were stained with hematoxylin and eosin. After clearing in xylene, the sections were mounted with neutral gum. The stained sections were examined under a light microscope, showing blue nuclei and eosinophilic cytoplasm. All the animal experiments complied with the guidelines of Tianjin Medical Experimental Animal Care, and animal protocols were approved by the institutional Animal Care and Use Committee of Yi Shengyuan Gene Technology (Tianjin) Co., Ltd (protocol number YSY-DWLL-2023,358).

2.12. Statistical analysis

Following the identification and exclusion of outliers, data are expressed as means ± standard deviations (SD). Results were evaluated using one-way ANOVA accompanied by Tukey's test. Statistical significance was set at * $p < 0.05$, ** $p < 0.01$ and *** $p < 0.001$. Data analysis was performed using Origin and GraphPad software.

3. Results and discussion

3.1. Synthesis and self-assembly of bottlebrush block copolymers

Amphiphilic block copolymers can self-assemble into two distinct nanostructures, nanomicelles (also known as micelles) and nanovesicles (also known as vesicles), both of which are suitable for delivering therapeutic agents. The morphological outcome of self-assembly (micelles or vesicles) is fundamentally determined by the growth mechanism of the polymer segments. Micelle formation represents the thermodynamically favored morphology in self-assembly. Vesicle formation requires precise molecular engineering of the copolymer composition to achieve stable nanostructures.

Initially, two copolymers of poly(D,L-lactic acid)-Dextran with identical copolymer composition were synthesized and subjected to self-assembly: the bottlebrush-type $(PDLLA_{20})_4$ $_g$-$Dex2K_{10}$ and the linear $PDLLA_{80}$-$Dex2K_{10}$. As demonstrated in our previous publication, the bottlebrush-type copolymer formed vesicles, whereas the linear $PDLLA_{80}$-$Dex2K_{10}$ self-assembled into micelles. Since the MENPs to be encapsulated in this study are hydrophilic, and micelles cannot effectively encapsulate hydrophilic particles, the linear $PDLLA_{80}$-$Dex2K_{10}$ was unsuitable as a reference system. Therefore, we selected another linear copolymer based on poly(L-lactic acid)-Dextran($PLLA_{80}$-$Dex2K_{10}$) as the vesicle-based reference system. This copolymer shares an identical composition with the bottlebrush-type $(PDLLA_{20})_4$ $_g$-$Dex2K_{10}$, and our prior work has confirmed its ability to self-assemble into vesicles (Table S1).

The general synthetic procedure for preparing bottlebrush block copolymers is illustrated in Figure S1. The degree of polymerization (DP), graft density, and molecular weight of the copolymers were determined by ^{1}HNMR analysis (Figure S1). TEM imaging revealed that both the bottlebrush $(PDLLA_{20})_4$ $_g$-$Dex2K_{10}$ and the conventional linear $PLLA_{80}$-g-$Dex2K_{10}$ copolymers self-assembled into vesicular structures (Fig. 1a). DLS measurements showed nearly identical hydraulic diameters of 196 nm and 198 nm for the two vesicles (Fig. 1b). In addition, the zeta potential of the two vesicles was about −14 mV (Figure S2).

3.2. Structure stability and cleavability of self-assembling vesicles

During systemic delivery, vesicles face multiple challenges, including infinite dilution, hemodynamic shear stress, and biointeractions with blood components. The optimal vesicle must withstand these destabilizing factors while maintaining structural stability. The critical vesicle concentration (CVC) was determined to assess vesicle resistance to infinite dilution. The ratio of fluorescence intensities between the third and first vibronic peaks of pyrene (I_3/I_1) provides a precise measure of the local polarity surrounding the pyrene molecules. Upon encapsulation within vesicles, the I_3/I_1 value of pyrene increases sharply, thus allowing determination of the CVC. As shown in Fig. 1c, bottlebrush vesicles and classical PLLA vesicles exhibit analogous dilution stability, with CVC of ~0.01 mg/mL.

A shear simulation experiment was further conducted to assess vesicles' structural stability [12–14]. Coumarin 6 was encapsulated in vesicles, and shear-induced drug leakage was quantified under controlled stress conditions. As shown in Fig. 1d, the concentration of released coumarin 6 from classical PLLA vesicles exhibited a time-dependent increase, indicating structural instability under shear stress. In contrast, bottlebrush vesicles maintained consistently low coumarin 6 release levels under identical shear conditions, confirming superior shear resistance and structural stability. Anionic surfactants can disrupt the entanglement of hydrophobic chains within the vesicle shell, while cationic surfactants and electrolytes can cause swelling of the hydrophobic chain stacking within the vesicle shell. All three agents can potentially induce vesicle shell disintegration [15,16,25]. The structural stability of vesicles in surfactant and electrolyte environments was investigated (Fig. 1e). Classical PLLA vesicles retained structural integrity when exposed to NaCl and anionic surfactant SDS solution. However, upon addition of cationic surfactant DDBAC, the PLLA vesicle dispersion exhibited increased upper-phase transmittance accompanied by bottom precipitate formation, confirming structural disruption. Conversely, bottlebrush vesicles retained exceptional structural integrity when exposed to NaCl, anionic surfactant SDS, and cationic DDBAC.

The cleavability of vesicles in response to reactive oxygen species (ROS) presents another critical challenge for achieving inflammation-targeted magnetoelectric stimulation therapy. Conventional PLLA

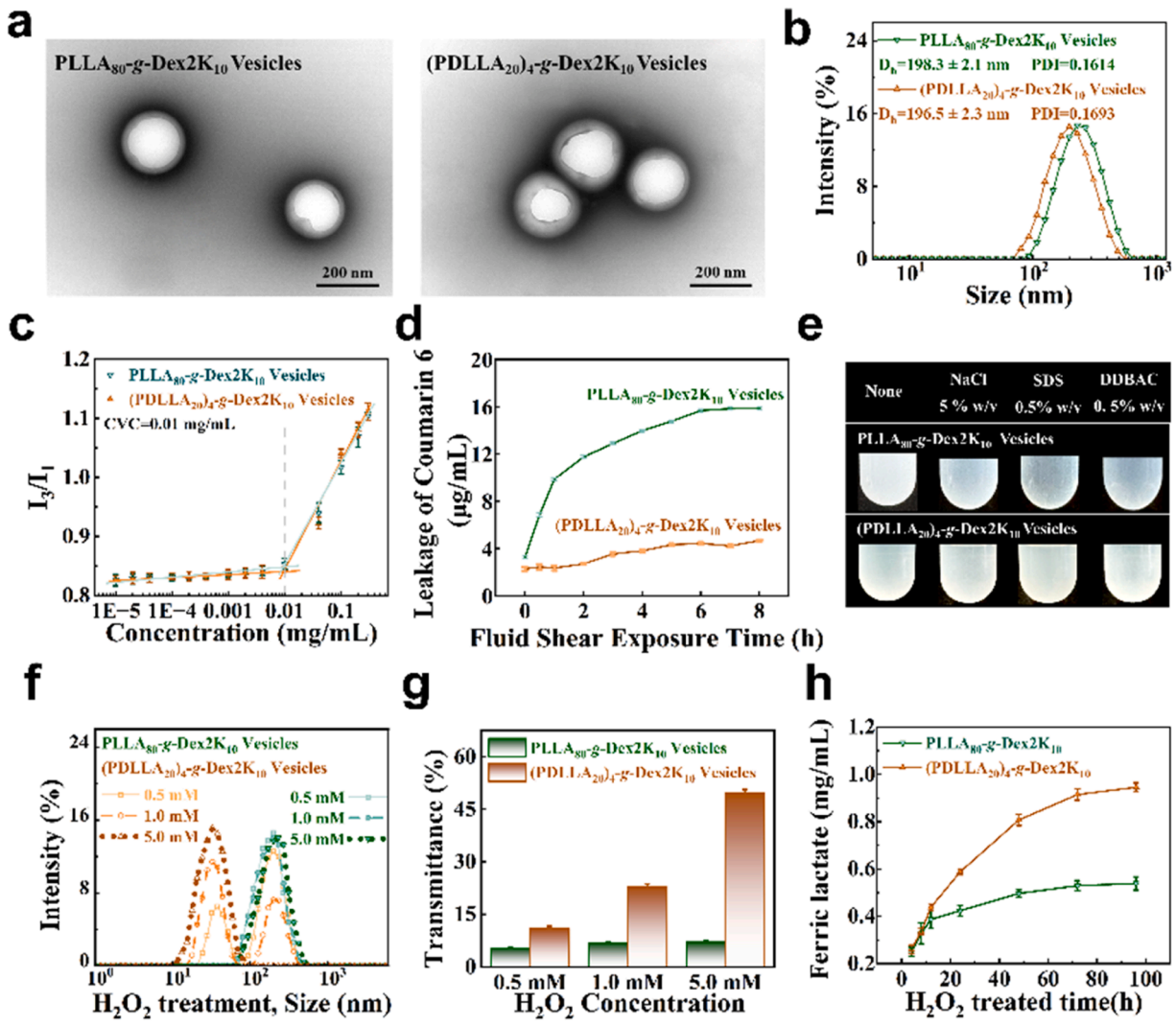

Fig. 1. Structure stability and cleavability of vesicles. a) TEM image (uranyl acetate negative staining, 120 kV). Scale bar: 200 nm. b) Hydrodynamic size distribution measured by DLS. c) Determination of the Critical Vesicle Concentration (CVC) by the pyrene fluorescence method. d) Leakage profile of coumarin 6-loaded vesicles under fluid shear stress. e) Structural stability of vesicles upon treatment with 5% w/v NaCl, 0.5% w/v SDS, and 0.5% w/v DDBAC. f) Size variation of vesicles after 0.5 mM, 1,0 mM, and 5.0 mM H_2O_2 treatment. g) Transmittance changes of vesicles after H_2O_2 treatment. h) Determination of lactic acid content in the cleavage products after treatment with 0.5 H_2O_2 mM.

vesicles exhibited only minor changes in both size and transmittance after treatment with H_2O_2 at different concentrations, indicating a limited cleavage response to H_2O_2. Specifically, while conventional PLLA vesicles showed only minor alterations in size and transmittance upon H_2O_2 treatment, indicating a weak cleavage response, PDLLA bottlebrush vesicles underwent significant cleavage when exposed to 0.5 mM H_2O_2, a concentration reported in the literature as physiologically relevant [18–21].

According to relevant literature, the ROS-responsive degradation of polylactic acid is primarily achieved through auto-catalytic hydrolytic degradation. In an H_2O_2 environment, superoxide ions can act as nucleophiles to attack organic ester groups, leading to their cleavage. This process mainly follows a bimolecular nucleophilic substitution pathway, converting the ester groups into the alcohols and carboxylic acids, while generating anionic end groups of varying chain lengths. These reactive anions subsequently attack the polymer backbone via transesterification, resulting in a rapid decrease in molecular weight until thermodynamic equilibrium is reached [32–34]. It is inferred that, in comparison with the chain packing and entanglement of linear polymer chains of the same molecular weight, the bottlebrush PDLLA polymer in this study exhibits extended conformations due to steric hindrance from the side chains, resulting in reduced chain entanglement and enhanced overall flexibility of the macromolecular chain. More importantly, the extended side chains provide more accessible sites for interaction with water molecules, free radicals, and ions, which may enable bottlebrush PDLLA to exhibit superior H_2O_2-responsive disassembly performance.

With increasing H_2O_2 concentration, a substantial number of small particles emerged, and a notable increase in transmittance was simultaneously observed, suggesting extensive vesicle rupture (Fig. 1f-g, Figure S3). Consistent with these observations, the rapid and abundant release of lactic acid further verified the superior cleavage efficiency of the PDLLA bottlebrush vesicles (Fig. 1h).

The above experimental results can be attributed to the distinctive steric repulsion effect inherent in bottlebrush polymers. The unique steric interactions among the side chains in PDLLA bottlebrushes give rise to two key physical properties: an extended backbone conformation and reduced entanglement of side chains. The extended backbone imparts a cylindrical morphology and enhances mechanical robustness, while the limited interchain entanglement facilitates nucleophilic attack on the ester groups, leading to their cleavage [25–27]. This combination achieves an optimal balance between vesicle structural stability and radical-mediated cleavability, which facilitates the targeted release of

MENPs in the inflammatory region, thereby advancing the objective of precise neurological stimulation therapy.

3.3. Preparation and characterization of magnetoelectric vesicles

TEM analysis coupled with EDS of the CFO-BTO MENPs confirmed that the monodispersed CFO core was encapsulated by the BTO shell (Fig. 2a-b, Figure S4). TEM images show MENPs aggregates formed during sample drying, not reflecting their true dispersion in water. In the aqueous phase, agglomeration is much lower. In this study, MENPs were dispersed in DMSO for co-assembly, where they exhibit better size stability and no rapid sedimentation, which facilitates encapsulation (Figure S2). XRD results further revealed the crystalline phases of the CFO-BTO MENPs, indicating a spinel structure for the CFO core and a perovskite structure for the BTO shell (Fig. 2c).

Additionally, the contents of cobalt, iron, barium, and titanium in the

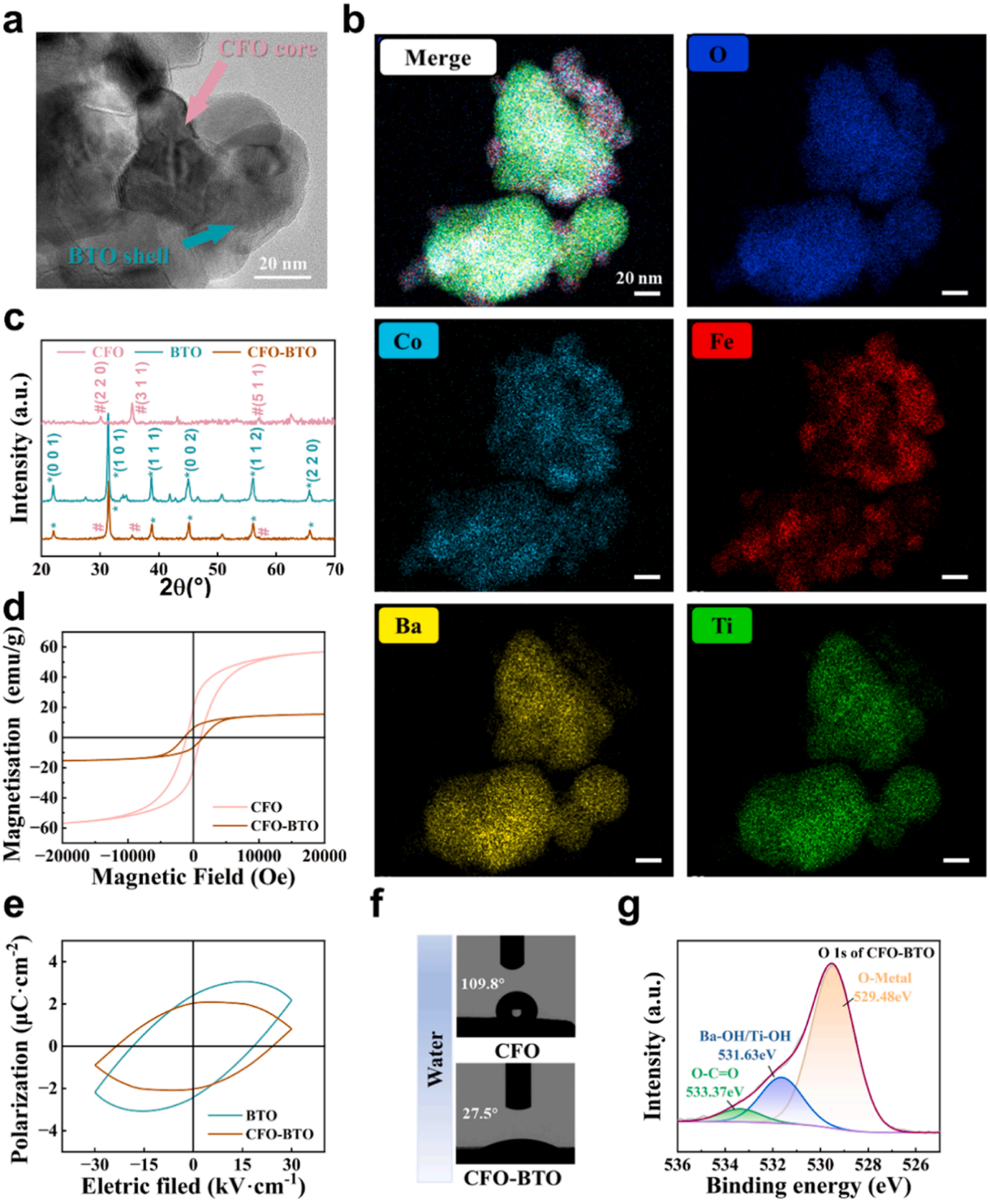

Fig. 2. Characterization of CFO-BTO MENPs. a) TEM image acquired without negative staining (120 kV, Scale bar: 20 nm). b) EDS elemental mapping of Co, Fe, Ba, Fe, and O elements. Scale bar: 20 nm. c) XRD pattern of CFO, BTO, and CFO-BTO(with Cu Kα radiation). d) Magnetic hysteresis loops measured at 300 K with a magnetic field sweep between ±20 kOe. e) Ferroelectric hysteresis loops. f) Water contact angles. g) High-resolution XPS spectrum.

CFO–BTO MENPs were analyzed by inductively coupled plasma optical emission spectrometry (ICP-OES). The results indicated that the CFO phase accounted for 67.37% of the composition, while the BTO phase constituted 32.63% (Figure S13).

Fig. 2d summarizes the magnetic properties of the CFO-BTO MENPs, with a saturation magnetization of 6.3 emu/g and a coercivity of 1093.3 Oe. The ferroelectric properties presented in Fig. 2e exhibit a remanent polarization of 2.2 μC/cm^2 and a coercive field of 24.2 kV/cm. Additionally, the d_{33} piezoelectric coefficient of CFO-BTO MENPs was measured as 41.86 × 10^{-12}C/N (Figure S5). These results are consistent with earlier observations in the literature [35–37]. Furthermore, surface contact angle measurements indicate that CFO exhibits a hydrophobic surface, whereas CFO-BTO MENPs demonstrate marked hydrophilicity (Fig. 2f). This change is attributed to the presence of hydrophilic hydroxyl groups (-OH) on the CFO-BTO MENPs surface, as confirmed by XPS analysis. The O 1 s spectrum of the CFO-BTO MENPs exhibits not only a lattice oxygen peak at 529.5 eV but also a distinct hydroxyl peak at 531.6 eV, indicating the presence of coordinated hydroxyl groups on the nanoparticle surface (Fig. 2g, Figure S6).

However, the poor colloidal stability of CFO-BTO MENPs (hereinafter referred to as MENPs) causes rapid aggregation in water through van der Waals, thermodynamic, and magnetic interactions, resulting in micron-scale precipitates (Fig. 3g). To address this issue, we encapsulated MENPs within vesicles self-assembled from a PDLLA–Dextran bottlebrush block copolymer, yielding magnetoelectric vesicles (designated as BB-MEVs). The system comprising bottlebrush polymer vesicle-loaded MENPs was designated as BB-MEVs. In this platform, bottlebrush polymer vesicles are employed as carriers for the delivery of MENPs. When subjected to an alternating magnetic field, localized electrical signals are generated by the encapsulated MENPs, thereby enabling precise stimulation and targeted therapy of specific neurons. (Fig. 3g, Figure S7).

A systematic evaluation of the BB-MEVs was subsequently conducted. It is worth noting that the MENPs synthesized in this study exhibit significantly greater size stability in DMSO than in water. Prior to self-assembly, they remain stably dispersed in DMSO without rapid sedimentation, which facilitates the encapsulation process (Figure S2). Fig. 3a suggests a high loading of MENPs within the polymeric vesicles,

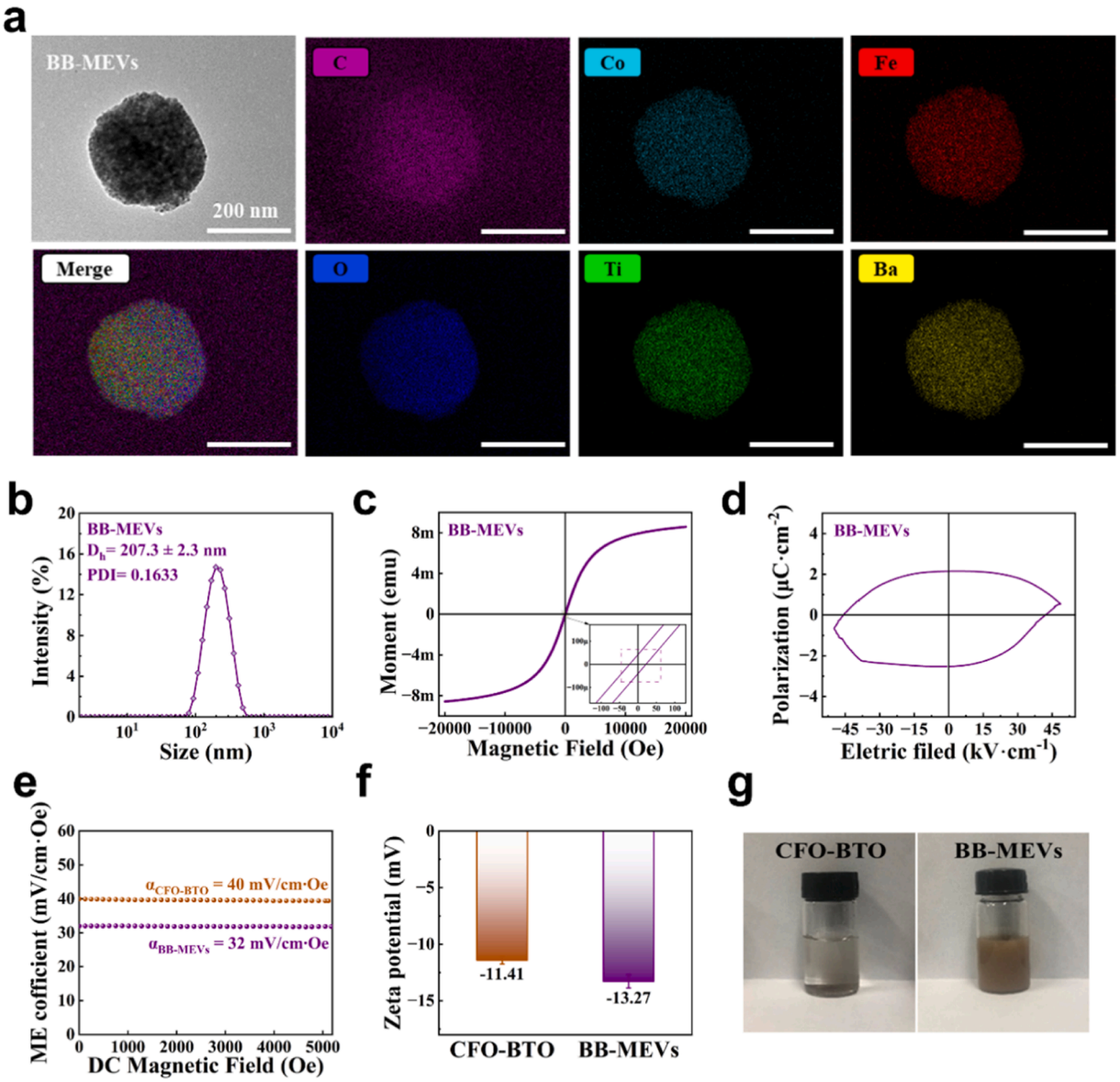

Fig. 3. Characterization of bottlebrush-based magnetoelectric vesicles (BB-MEVs). a) TEM image and corresponding EDS elemental mapping (t200 kV. Scale bar: 200 nm). b) Hydrodynamic size distribution. c) Magnetic hysteresis loop. d) Ferroelectric hysteresis loops. e) Magnetoelectric coefficient. f) Zeta potential. g) Stability of polymer vesicles against NaCl, SDS, and DDBAC.

while Figures S8 and S9 indicate a relatively lower encapsulation level. This discrepancy may be attributed to the broad size distribution of the MENPs, due to which larger aggregates cannot be effectively incorporated into the vesicles. To address this, after self-assembly, the dispersion was allowed to settle for 10 min, and a conventional magnet was used to adsorb and remove the unencapsulated MENPs that had precipitated. Only the upper yellowish vesicle suspension was collected for subsequent experiments (Fig. 3*g*). Furthermore, based on ICP-MS analysis of the dried magnetoelectric vesicle powder (Figure S9), the weight-based loading efficiency of MENPs was calculated from the iron and titanium contents to be approximately 15 wt%. TEM observation and EDS elemental mapping confirm the successful encapsulation of MENPs within the vesicles (Fig. 3a, Figure S8).

BB-MEVs have a hydrodynamic diameter of approximately 207 nm (Fig. 3b). The zeta potential of BB-MEVs was determined to be −13.27 ± 0.59 mV. The loading capacity of CFO-BTO in BB-MEVs was determined to be 15.2 ± 0.3% by mass using ICP-OES (Figure S9). Magnetic hysteresis measurements in Fig. 3c indicate that BB-MEVs exhibit low coercivity of approximately 18 Oe, suggesting rapid magnetic moment reversal under alternating magnetic fields. The BB-MEVs exhibit a remanent polarization of 2.1 μC/cm^2 and a coercive field of 42.1 kV/cm (Fig. 3d). The magnetoelectric coefficient was measured under conditions suitable for in vivo brain stimulation, specifically using a 6 mT AC magnetic field at a test frequency of 140 Hz (refer to Section 4.10), while a DC magnetic field was swept parallel to the sample plane over a range of 0–5 kOe.

The results showed that the electrical signal output exhibited low dependence on the input DC magnetic field, which aligns with prior reports on CFO-BTO magnetoelectric nanoparticles (Fig. 3e) [6]. This behavior can be explained by the characteristic of classical magnetoelectric materials, whose magnetoelectric coefficient increases sharply near the mechanical resonance frequency but remains relatively stable when operated away from resonance [3,6]. In this study, the carrier magnetic signal frequency used (140 Hz) is far below the resonant frequency range of nanoscale magnetoelectric nanoparticles (which is in the gigahertz range), thus operating in a non-resonant state. It is precisely this non-resonant coupling mechanism that leads to the observed lower magnetoelectric coefficient. While applying large AC magnetic fields can approach the maximum ME response, this strategy simultaneously generates substantial heat and requires powerful coil systems, thereby diminishing its prospects for in vivo therapeutic applications. Although the nano-scale MENPs exhibit a lower magnetoelectric response under this condition, the resulting electrical signals have been demonstrated to generate sufficient output to exceed the threshold required for effective neuromodulation. The magnetoelectric coupling coefficient of the BB-MEVs was measured to be 32 mV/cm·Oe (Fig. 3e), closely matching the values of CFO-BTO MENPs [6].

3.4. Magnetoelectric stimulation of neuronal cells via BB-MEVs

SH-SY5Y cells were treated with BB-MEVs for 24 hours across a range of concentrations. Subsequent CCK-8 analysis revealed minimal cytotoxicity, with cell viability consistently exceeding 95% under all conditions, confirming the high biocompatibility of BB-MEVs (Fig. 4a). Magnetoelectric stimulation was applied at an intensity of 6 mT and a frequency of 140 Hz using a custom-built system (Figure S10). When neurons are activated by magnetoelectric stimulation, voltage-gated calcium channels open, allowing a massive influx of extracellular

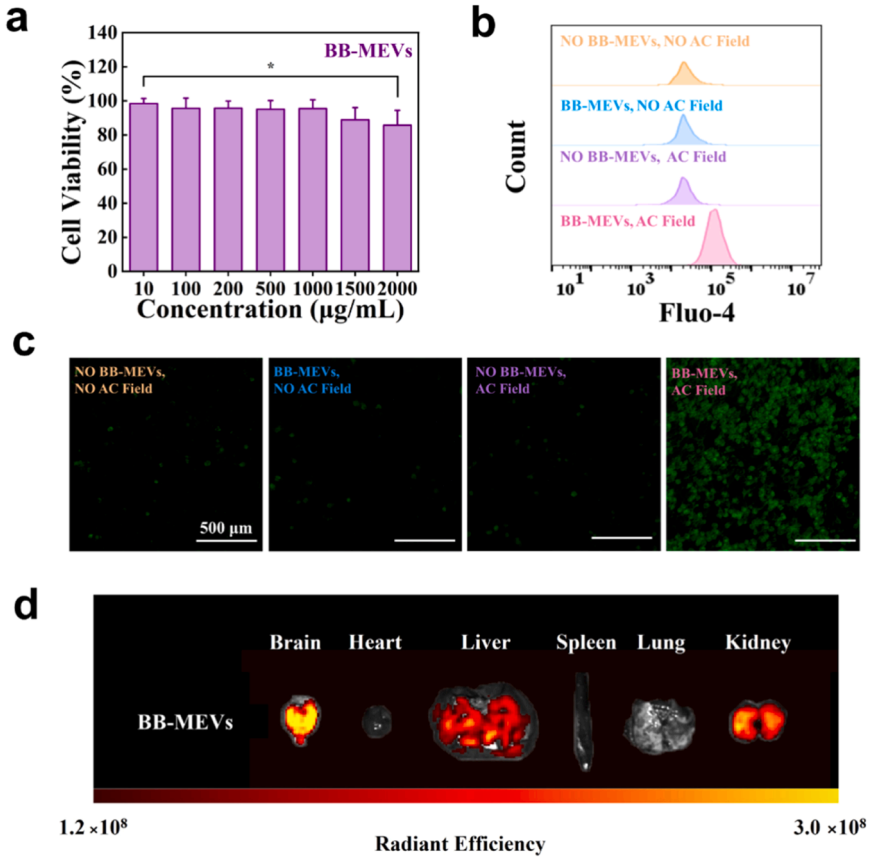

Fig. 4. Magnetoelectric stimulation of SH-SY5Y cells by BB-MEVs. a) Cytotoxicity assessment of BB-MEVs. b) Flow cytometry analysis showing Ca^{2+} signal in SH-SY5Y cells. Cell loading quantities and the number of flow cytometry acquisition events were normalized. c) Fluorescence microscopy images of Ca^{2+} signal in SH-SY5Y cells. The fluorescent images shown were captured from culture areas with approximately 70–80% confluency and exhibiting healthy cell morphology. d) In vivo distribution images following intranasal administration of BB-MEVs.

calcium ions into the cytoplasm. This influx was monitored using the fluorescent probe Fluo-4 AM, as changes in intracellular Ca^{2+} concentration indirectly reflect the strength of neuronal electrophysiological activity, thus enabling the evaluation of the magnetoelectric stimulation effect. This approach is supported by previous studies confirming that CFO-BTO MENPs can generate sufficient electrical output to modulate neural cells [3,6]. As shown in Fig. 4b, intracellular Ca^{2+} levels following magnetoelectric stimulation were quantified using flow cytometry with the Fluo-4 AM fluorescent probe. Intracellular Ca^{2+}levels exhibited no significant change upon exposure to BB-MEVs or AC fields alone. However, magnetoelectric stimulation via BB-MEVs induced a pronounced elevation in Ca^{2+} concentrations, resulting in an approximately fourfold increase compared to control groups treated solely with BB-MEVs or AC fields. Consistent with these results, inverted fluorescence microscopy observations confirmed the effective modulation of neuronal activity following magnetoelectric stimulation with BB-MEVs (Fig. 4c).

Prior to magnetoelectric stimulation therapy, the intracranial delivery potential of BB-MEVs was assessed via *ex vivo* fluorescence imaging. Coumarin 6-loaded BB-MEVs were intranasally administered to rats. Major organs, including the brain, heart, liver, spleen, lungs, and kidneys, were harvested and systematically examined 2 hours post-administration (Fig. 4d). Imaging results showed pronounced fluorescence accumulation in the brain tissue, demonstrating the efficient brain delivery capability of BB-MEVs.

3.5. Deep brain stimulation via BB-MEVs in epileptic rats

An acute model was induced using lithium-pilocarpine kindling, which resulted in sustained seizures [31]. Seizure frequency and duration were recorded for 2 hours after pilocarpine administration (Fig. 5a). During stimulation, the magnetic field was confined to the head, while the rest of the body was magnetically shielded to ensure localized magnetoelectric stimulation specific to the brain (Fig. 5b). Real-time EEG recordings revealed that BB-MEVs/4AC treatment promptly suppressed abnormal brain activity in the epileptic rats, as evidenced by reduced local field potential and power density compared to epileptic rats (Fig. 5c, Figure S11a). Epilepsy rats treated with BB-MEVs/4AC showed a suppressed high-frequency LFP signal in the spectral analysis, indicating the suppressed neuron activity after therapy (Fig. 5d, Figure S11b). The epilepsy group exhibited rapid epileptogenesis, with 36 seizures occurring within a 2-hour period. Treatments with both BB-MEVs/2AC and BB-MEVs/4AC significantly reduced seizure frequency. Notably, the BB-MEVs/4AC group displayed fewer than 6 seizures during the observation period (Fig. 5e). We further investigated the duration of epileptic seizures across all groups. The epilepsy group and the AC field group exhibited average seizure durations of approximately 200 s. In contrast, the BB-MEVs stimulation groups showed a substantial reduction, decreasing to approximately one-tenth of that in the epilepsy group. Specifically, seizures in the BB-MEVs/4AC group lasted nearly 15 $\pm$ 4 s (Fig. 5f). These results indicate that BB-MEVs stimulation significantly reduces seizure activity, highlighting its potential as a therapeutic strategy for modulating neural hyperexcitability in epilepsy. Open-field testing performed 24 hours post-stimulation revealed that BB-MEVs/4AC-treated rats displayed normal exploratory behavior, indicated by a significant increase in movement trajectories relative to the epilepsy group. Weight monitoring revealed significant body weight loss in the epilepsy group and AC field-treated groups, whereas animals treated with BB-MEVs exhibited weight recovery (Fig. 5g-k). The improvements in both body weight and behavioral parameters demonstrate that BB-MEVs-mediated neurostimulation effectively mitigates seizure-induced physical deterioration.

During an epileptic seizure, neuronal populations display synchronized, high-frequency burst firing, triggering a sharp rise in intracellular calcium levels. This calcium influx activates downstream signaling pathways, leading to rapid upregulation of c-Fos protein. As an established marker of neuronal activation, c-Fos is widely used to map seizure foci and related neural circuits [6]. As shown in Fig. 6a, a marked increase in c-Fos protein expression was observed following epilepsy induction, indicating a state of neuronal hyperactivation. In animals treated with BB-MEVs, c-Fos expression was significantly reduced to levels comparable to those in healthy controls (Figure S15a-d). These results demonstrate that repeated magnetoelectric stimulation effectively modulates aberrant neuronal circuit activity in rats, thereby suppressing the propagation of epileptic activity. The therapeutic efficacy of BB-MEVs was further evaluated using Nissl staining. In the epilepsy group, substantial neuronal loss was observed, along with irregular morphology and disorganized arrangement of Nissl bodies, suggesting impaired neural function in the hippocampus (Fig. 6b). In contrast, the magnetoelectric stimulation group exhibited a marked increase in the number of intact Nissl bodies and a more regular organization, indicating an improved neuropathological condition (Figure S15e-f).

Following magnetoelectric stimulation, brain tissues were analyzed using Prussian blue staining, a histochemical method specific for ferric iron detection, to achieve precise mapping of MENPs distribution within the brain tissue [38]. Prussian blue staining revealed distinct iron deposits distributed across the hippocampus, cerebral cortex, and thalamus (Fig. 6c). These regions are recognized for demonstrating neuroinflammatory activity in both epileptogenic brain regions in humans and animal models of epilepsy [39–42]. Brain tissues from healthy and epileptic model rats were analyzed by Prussian blue staining. The analysis revealed no observable iron deposition in the hippocampal region, cortical area, or thalamic nuclei in either group (Figure S14). Based on these findings, it is reasonable to infer that BB-MEV likely achieved targeting toward higher inflammatory regions in epileptic rats. Notably, micron-scale iron accumulations were consistently observed in these neuroinflammatory regions. These findings appear to be consistent with the occurrence of ROS cleavage-induced MENPs release and subsequent MENPs aggregation, which might be interpreted as suggestive evidence for the potential of BB-MEVs to localize within neuroinflammatory regions. The reassembled micron-scale MENPs aggregates, if formed, could conceivably possess magnetoelectric coupling properties that differ from those of their nano-sized counterparts, and it is possible that such properties might, under appropriate conditions, have a bearing on the effectiveness of neuromodulation therapy [6,7,43]. Furthermore, H&E staining showed negligible inflammatory responses across major organs, supporting the systemic biosafety of BB-MEVs (Figure S12).

4. Conclusion

The competing requirements of systemic delivery stability and lesion-specific ROS-responsive cleavability create a key engineering challenge for magnetoelectric nanoparticles delivery nanovehicles in epilepsy deep brain stimulation applications. This study describes the development of a PDLLA bottlebrush block copolymer that may influence main-chain extension and side-chain entanglement. Such architectural features could conceivably contribute to the mechanical stability and ROS responsiveness of self-assembled vesicles for MENP delivery. When compared with traditional PLLA-based vesicles, the BB-MEVs appear to exhibit certain differences in stability and cleavability that may merit further consideration. Under appropriate conditions, these vesicles might be capable of supporting in situ neural stimulation in deep brain regions. It is conceivable that such stimulation could modulate neural circuit activity, influence electrophysiological function, or affect seizure-related behaviors in a rat model of epilepsy, though the extent and significance of these effects remain to be elucidated. The present work may offer preliminary insights that could be of relevance to the development of wireless and noninvasive neural nanotechnology, and might have implications for future research on brain–machine interfaces in the context of neurological disorders.

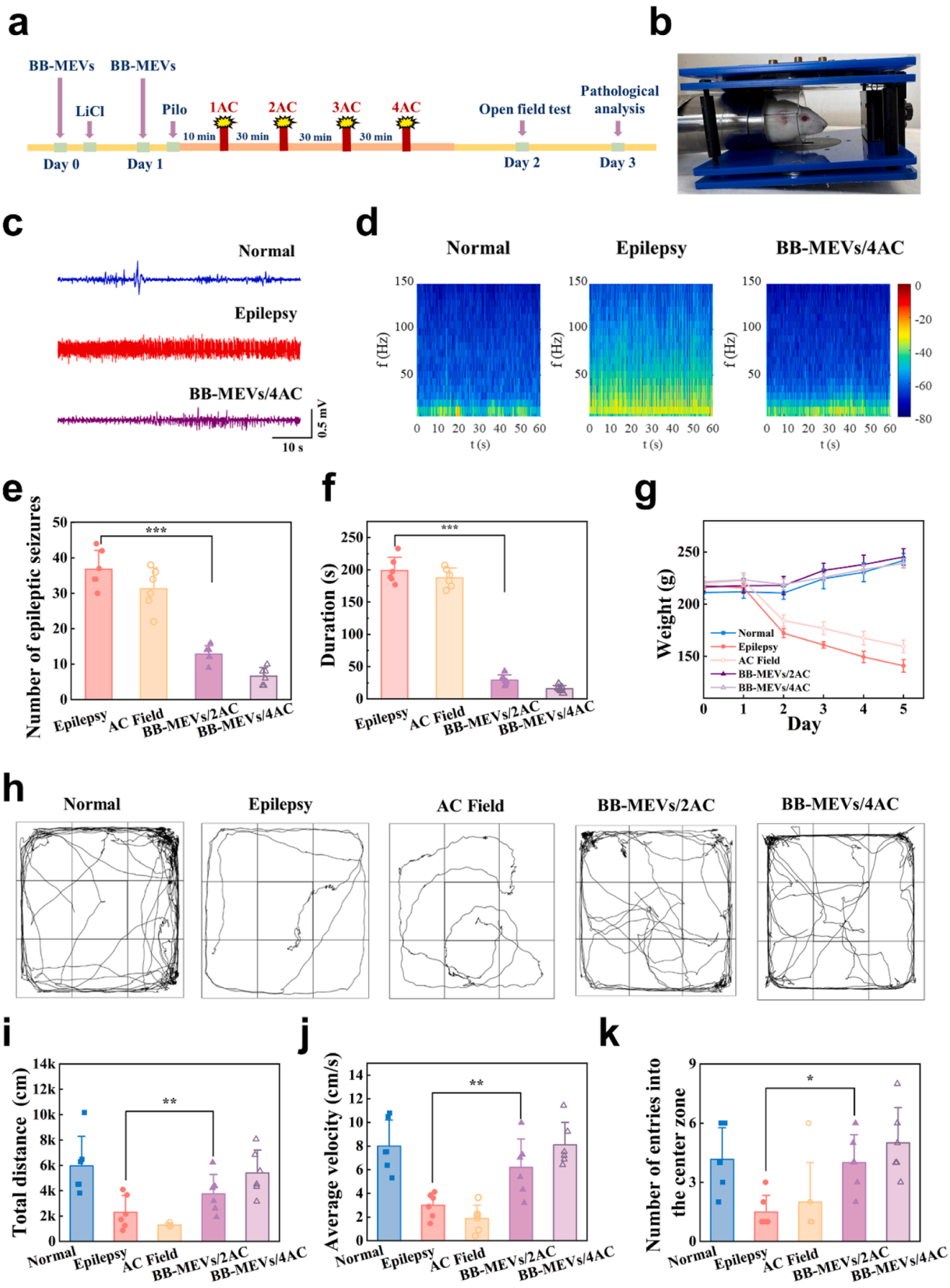

Fig. 5. In vivo magnetoelectric stimulation of BB-MEVs against epilepsy. a) Schematic of the experimental timeline for epilepsy magnetoelectric treatment. b) Magnetoelectric brain stimulation with bodily shielding. c-d) Representative local field potential (LFP) signal (c) and corresponding time-frequency analysis (d). e) Number of epileptic seizures. f) The duration of epileptic seizures. g) Body weight changes of rats. h) Representative movement trajectories of rats during a 10-minute open-field test. i–k) Quantitative analysis of open-field behaviors: total distance moved (i), average velocity (j), and number of entries into the center zone (k). One-way ANOVA with Tukey's post hoc test showed a significant difference between the model and stimulation groups (*$p < 0.05$).

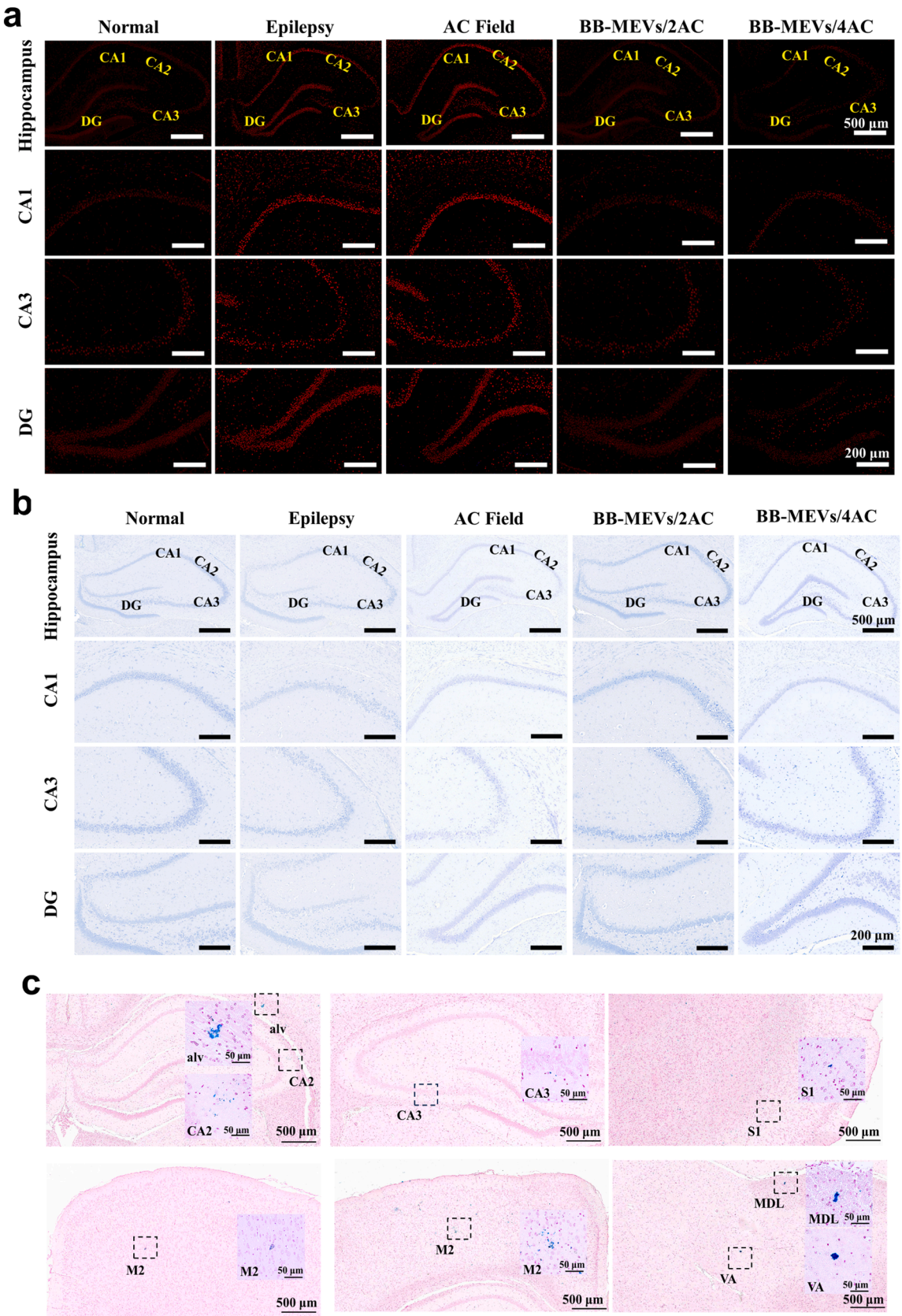

Fig. 6. a) Immunostaining of c-Fos protein in neurons associated with neuronal activation. b) Representative Nissl-stained sections to examine the morphology and structural integrity of neurons. c) Prussian blue staining to validate the distribution of BB-MEVs in targeted brain regions, including the hippocampus (CA2 and CA3), Alveus (alv), primary somatosensory cortex (S1), secondary motor cortex (M2), mediodorsal thalamic nucleus (MDL), and ventral anterior nucleus (VA).

CRediT authorship contribution statement

Yiran Chen: Writing – original draft, Data curation. **Meng Xiao:** Writing – review & editing, Visualization, Conceptualization. **Yage Sun:** Writing – review & editing. **Lu Wang:** Resources. **Zhou Li:** Writing – review & editing, Funding acquisition. **Fengying Dai:** Writing – original draft, Project administration, Conceptualization.

Declaration of competing interest

The authors declare that they have no known competing financial interests or personal relationships that could have appeared to influence the work reported in this paper.

Acknowledgements

Y. Chen and M. Xiao contributed equally to this work. The authors gratefully acknowledge the support for this work from Brain Science and Brain-like Intelligence Technology-National Science and Technology Major Project (2021ZD0201600), Hebei Natural Science Foundation (Grant No. B2025110015), Cangzhou Natural Science Foundation (Grant No. 23241001007 N), the National Science Foundation of China (Grant No. T2125003, U25A20417, 52403212,), Beijing Natural Science Foundation (L245015, Z240022, 25JL006).

Supplementary materials

Supplementary material associated with this article can be found, in the online version, at doi:10.1016/j.actbio.2026.06.048.

Data availability : Research data are not shared.

References

[1] J.K. Kleen, V.R. Rao, Managing Neurostimulation for epilepsy, Deep Brain Stimulation Management, Cambridge University Press, 2022, pp. 177–197.
[2] Q. Ren, H. Wu, Y. Zhang, J. Dai, Z. Chang, J. Nie, B. Wang, Y. Fang, Nongenetic precise neuromodulation and spatiotemporal neuroprotection for epilepsy therapy via rationally designed multifunctional nanotransducer, ACS Nano 18 (26) (2024) 16853–16866.
[3] F. Alrashdan, K. Yang, J.T. Robinson, Magnetoelectrics for implantable bioelectronics: progress to date, Accounts Chem. Res. 57 (20) (2024) 2953–2962.
[4] Y. Zhang, S. Chen, Z. Xiao, X. Liu, C. Wu, K. Wu, A. Liu, D. Wei, J. Sun, L. Zhou, H. Fan, Magnetoelectric nanoparticles incorporated biomimetic matrix for wireless electrical stimulation and nerve regeneration, Adv. Healthc. Mater. 10 (16) (2021) e2100695.
[5] K. Yue, R. Guduru, J. Hong, P. Liang, M. Nair, S. Khizroev, Magneto-electric nano-particles for non-invasive brain stimulation, PLoS One 7 (9) (2012) e44040.
[6] K.L. Kozielski, A. Jahanshahi, H.B. Gilbert, Y. Yu, O. Erin, D. Francisco, F. Alosaimi, Y. Temel, M. Sitti, Nonresonant powering of injectable nanoelectrodes enables wireless deep brain stimulation in freely moving mice, Sci. Adv. 7 (3) (2021) eabc4189.
[7] Y. Zhang, X. Wu, J. Ding, B. Su, Z. Chen, Z. Xiao, C. Wu, D. Wei, J. Sun, F. Luo, H. Yin, H. Fan, Wireless-powering deep brain stimulation platform based on 1D-structured magnetoelectric nanochains applied in antiepilepsy treatment, ACS Nano 17 (16) (2023) 15796–15809.
[8] J.C. Chen, P. Kan, Z. Yu, F. Alrashdan, R. Garcia, A. Singer, C.S.E. Lai, B. Avants, S. Crosby, Z. Li, B. Wang, M.M. Felicella, A. Robledo, A.V. Peterchev, S.M. Goetz, J. D. Hartgerink, S.A. Sheth, K. Yang, J.T. Robinson, A wireless millimetric magnetoelectric implant for the endovascular stimulation of peripheral nerves, Nat. Biomed. Eng. 6 (6) (2022) 706–716.
[9] M. Taheri, S. Maaref, A. Kantzas, S. Bryant, S. Trudel, Improving the colloidal stability of PEGylated $BaTiO_3$ nanoparticles with surfactants, Chem. Phys. 564 (2023) 111701.
[10] A. Sood, M. Desseigne, A. Dev, L. Maurizi, A. Kumar, N. Millot, S.S. Han, A comprehensive review on barium titanate nanoparticles as a persuasive piezoelectric material for biomedical applications: prospects and challenges, Small 19 (12) (2023) e2206401.
[11] Z. Tian, X. Wang, L. Shu, T. Wang, T.H. Song, Z. Gui, L. Li, Preparation of nano $BaTiO_3$-based ceramics for multilayer ceramic capacitor application by chemical coating method, J. Am. Ceram. Soc. 92 (4) (2009) 830–833.
[12] H. Zhang, Z. He, C. Fu, P. Pan, Y. Zhu, M. Xu, S. Deng, G. Ying, Y. Shen, Dissociation of polymeric micelle under hemodynamic shearing, Nano Today 45 (2022) 101517.
[13] L.D. Casa, D.H. Deaton, D.N. Ku, Role of high shear rate in thrombosis, J. Vasc. Surg. 61 (4) (2015) 1068–1080.
[14] Z. Shen, H. Ye, M. Kroger, Y. Li, Self-assembled core-polyethylene glycol-lipid shell nanoparticles demonstrate high stability in shear flow, Phys. Chem. Chem. Phys. 19 (20) (2017) 13294–13306.
[15] P. Chambon, A. Blanazs, G. Battaglia, S.P. Armes, How does cross-linking affect the stability of block copolymer vesicles in the presence of surfactant? Langmuir 28 (2) (2012) 1196–1205.
[16] M.M. Santore, D.E. Discher, Y.-Y. Won, F.S. Bates, D.A. Hammer, Effect of surfactant on unilamellar polymeric vesicles: altered membrane properties and stability in the limit of weak surfactant partitioning, Langmuir 18 (20) (2002) 7299–7308.
[17] L. Zhang, Q. Lu, X. Lv, L. Shen, B. Zhang, Z. An, In situ cross-linking as a platform for the synthesis of triblock copolymer vesicles with diverse surface chemistry and enhanced stability via RAFT dispersion polymerization, Macromolecules 50 (5) (2017) 2165–2174.
[18] X. Su, W. Zhuang, T. Yu, H. He, B. Ma, L. Chen, L. Yang, G. Li, Y. Wang, ROS and GSH dual-responsive GEM prodrug micelles for ROS-triggered fluorescence turn on bioimaging and cancer therapy, Adv. Mater. Interfaces 7 (13) (2020) 2000294.
[19] H. Wei, R.-X. Zhuo, X.-Z. Zhang, Design and development of polymeric micelles with cleavable links for intracellular drug delivery, Prog. Polym. Sci. 38 (3–4) (2013) 503–535.
[20] B. Parshad, S. Arora, B. Singh, Y. Pan, J. Tang, Z. Hu, H.K. Patra, Towards precision medicine using biochemically triggered cleavable conjugation, Comm. Chem. 8 (1) (2025) 100.
[21] G. Saravanakumar, J. Kim, W.J. Kim, Reactive-oxygen-species-responsive drug delivery systems: promises and challenges, Adv. Sci. 4 (1) (2017) 1600124.
[22] H. Hu, J. Wang, J. Ren, X. Li, B. Zhang, Z. Lv, F. Dai, Hydrophilic polymer driven crystallization self-assembly: an inflammatory multi-drug combination nanosystem against Alzheimer's disease, J. Mat. Chem. B 9 (39) (2021) 8272–8288.
[23] J. Ren, F. Jiang, S. Wang, H. Hu, B. Zhang, Y.P. Zhao, L. Chen, Z. Lv, F. Dai, Hydrophilic hindering and hydrophobic growing: a vesicle glycometabolism multi-drug combination therapeutic against Alzheimer's disease, Biomater. Sci. 9 (19) (2021) 6444–6460.
[24] F. Dai, X. Li, K. Lv, J. Wang, Y. Zhao, Combined core stability and degradability of nanomedicine via amorphous PDLLA-Dextran bottlebrush copolymer for Alzheimer's disease combination treatment, ACS Appl. Mater. Interfaces 15 (22) (2023) 26385–26397.
[25] W.F.M. Daniel, G. Xie, M. Vatankhah Varnoosfaderani, J. Burdyńska, Q. Li, D. Nykypanchuk, O. Gang, K. Matyjaszewski, S.S. Sheiko, Bottlebrush-guided polymer crystallization resulting in supersoft and reversibly moldable physical networks, Macromolecules 50 (5) (2017) 2103–2111.
[26] W.F. Daniel, J. Burdynska, M. Vatankhah-Varnoosfaderani, K. Matyjaszewski, J. Paturej, M. Rubinstein, A.V. Dobrynin, S.S. Sheiko, Solvent-free, supersoft and superelastic bottlebrush melts and networks, Nat. Mater. 15 (2) (2016) 183–189.
[27] G. Xie, M.R. Martinez, M. Olszewski, S.S. Sheiko, K. Matyjaszewski, Molecular bottlebrushes as novel materials, Biomacromolecules 20 (1) (2019) 27–54.
[28] M. Hales, C. Barner-Kowollik, T.P. Davis, M.H. Stenzel, Shell-cross-linked vesicles synthesized from block copolymers of Poly(D,L-lactide) and Poly(N-isopropyl acrylamide) as thermoresponsive nanocontainers, Langmuir 20 (25) (2004) 10809–10817.
[29] S. Munjal, N. Khare, C. Nehate, V. Koul, Water dispersible $CoFe_2O_4$ nanoparticles with improved colloidal stability for biomedical applications, J. Magn. Magn. Mater. 404 (2016) 166–169.
[30] P. Wang, E. Zhang, D. Toledo, I.T. Smith, B. Navarrete, N. Furman, A.F. Hernandez, M. Telusma, D. McDaniel, P. Liang, S. Khizroev, Colossal magnetoelectric effect in core-shell magnetoelectric nanoparticles, Nano Lett. 20 (8) (2020) 5765–5772.
[31] K.D. Phelan, U.T. Shwe, D.K. Williams, L.J. Greenfield, F. Zheng, Pilocarpine-induced status epilepticus in mice: a comparison of spectral analysis of electroencephalogram and behavioral grading using the Racine scale, Epilepsy Res. 117 (2015) 90–96.
[32] K.H. Lee, C.Y. Won, C.C. Chu, I. Gitsov, Hydrolysis of biodegradable polymers by superoxide ions, J. Polym. Sci. A Polym. Chem. 37 (18) (1999) 3558–3567.
[33] D. Rasselet, A. Ruellan, A. Guinault, G. Miquelard-Garnier, C. Sollogoub, B. Fayolle, Oxidative degradation of polylactide (PLA) and its effects on physical and mechanical properties, Eur. Polym. J. 50 (2014) 109–116.
[34] Y. Shen, B. Cao, N.R. Snyder, K.M. Woeppel, J.R. Eles, X.T. Cui, ROS responsive resveratrol delivery from LDLR peptide conjugated PLA-coated mesoporous silica nanoparticles across the blood-brain barrier, J. Nanobiotechnol. 16 (1) (2018) 13.
[35] R. Gao, Q. Zhang, Z. Xu, Z. Wang, W. Cai, G. Chen, X. Deng, X. Cao, X. Luo, C. Fu, Strong magnetoelectric coupling effect in $BaTiO_3$@$CoFe_2O_4$ magnetoelectric multiferroic fluids, Nanoscale 10 (25) (2018) 11750–11759.
[36] K. Shahzad, S. Mushtaq, M. Rizwan, W. Khalid, M. Atif, F.U. Din, N. Ahmad, R. Abbasi, Z. Ali, Field-controlled magnetoelectric core-shell $CoFe_2O_4$@$BaTiO_3$ nanoparticles as effective drug carriers and drug release in vitro, Mater. Sci. Eng. C-Mater. Biol. Appl. 119 (2021) 111444.
[37] R. Gao, Q. Zhang, Z. Xu, Z. Wang, G. Chen, C. Fu, X. Deng, W. Cai, Anomalous magnetoelectric coupling effect of $CoFe_2O_4$-$BaTiO_3$ binary mixed fluids, ACS Appl. Electron. Mater. 1 (7) (2019) 1120–1132.
[38] P.B. Balakrishnan, N. Silvestri, T. Fernandez-Cabada, F. Marinaro, S. Fernandes, S. Fiorito, M. Miscuglio, D. Serantes, S. Ruta, K. Livesey, O. Hovorka, R. Chantrell, T. Pellegrino, Exploiting unique alignment of cobalt ferrite nanoparticles, mild

hyperthermia, and controlled intrinsic cobalt toxicity for cancer therapy, Adv. Mater. 32 (45) (2020) e2003712.
[39] G. Terrone, F. Frigerio, S. Balosso, T. Ravizza, A. Vezzani, Inflammation and reactive oxygen species in status epilepticus: biomarkers and implications for therapy, Epilepsy Behav. 101 (2019) 106275.
[40] E. Aronica, P.B. Crino, Inflammation in epilepsy: clinical observations, Epilepsia 52 (Suppl 3) (2011) 26–32.
[41] A. Vezzani, S. Balosso, T. Ravizza, Neuroinflammatory pathways as treatment targets and biomarkers in epilepsy, Nat. Rev. Neurol. 15 (8) (2019) 459–472.
[42] E.A. van Vliet, E. Aronica, A. Vezzani, T. Ravizza, Review: neuroinflammatory pathways as treatment targets and biomarker candidates in epilepsy: emerging evidence from preclinical and clinical studies, Neuropathol. Appl. Neurobiol. 44 (1) (2018) 91–111.
[43] J. Choi, K.T. Nam, E.H. Sohn, Y. Seo, Macroscopic room-temperature magnetoelectricity in piezoelectric (core)-ferrimagnetic (shell) nanocomposites, ACS Nano 18 (44) (2024) 30681–30689.